Quantitative Ultrasound Characterization of Responses to Radiotherapy in Cancer Mouse Models

Roxana M. Vlad,[1,3] Sebastian Brand,[5] Anoja Giles,[3] Michael C. Kolios,[1,4] and Gregory J. Czarnota[1,2,3]

Abstract

Purpose: Currently, no imaging modality is used routinely to assess tumor responses to radiotherapy within hours to days after the delivery of treatment. In this study, we show the application of quantitative ultrasound methods to characterize tumor responses to cancer radiotherapy *in vivo,* as early as 24 hours after treatment administration.

Experimental Design: Three mouse models of head and neck cancer were exposed to radiation doses of 0, 2, 4, and 8 Gray. Data were collected with an ultrasound scanner using frequencies of 10 to 30 MHz. Ultrasound estimates calculated from normalized power spectra and parametric images (spatial maps of local estimates of ultrasound parameters) were used as indicators of response.

Results: Two of the mouse models (FaDu and C666-1) exhibited large hyperechoic regions at 24 hours after radiotherapy. The ultrasound integrated backscatter increased by 6.5 to 8.2 dB ($P < 0.001$) and the spectral slopes increased from 0.77 to 0.90 dB/MHz for the C666-1 tumors and from 0.54 to 0.78 dB/MHz for the FaDu tumors ($P < 0.05$), in these regions compared with preirradiated tumors. The hyperechoic regions in the ultrasound images corresponded in histology to areas of cell death. Parametric images could discern the tumor regions that responded to treatment. The other cancer mouse model (Hep-2) was resistant to radiotherapy.

Conclusions: The results indicate that cell structural changes after radiotherapy have a significant influence on ultrasound spectral parameters. This provides a foundation for future investigations regarding the use of ultrasound in cancer patients to individualize treatments noninvasively based on their responses to specific interventions.

In clinical oncology, tumor responses to treatment are still largely assessed using anatomic imaging measurements of reductions in tumor size. This can take several weeks to occur and with some therapies may not occur at all despite a positive functional response to treatment (1). Computed tomography, positron emission tomography, and combined computed tomography/positron emission tomography imaging have been used to assess tumor responses to cancer therapies typically 3 to 4 weeks after treatment initiation (2, 3). Dynamic contrast-enhanced magnetic resonance imaging measurements have been shown to correlate with immunohistochemical surrogates of tumor antiangiogenesis (4, 5) within the same time frame. Diffusion-weighted magnetic resonance imaging has been used clinically to measure therapy response in different type of cancers such as brain tumors (6), gastrointestinal cancers (7), and metastatic breast cancer (8). Dynamic contrast-enhanced Doppler ultrasound has predicted early tumor responses in isolated perfusion studies of limb sarcomas (9) within 1 to 7 days after therapy delivery. However, the use of such imaging modalities to monitor tumor responses to cancer therapies can be limited either by their cost (dynamic contrast-enhanced magnetic resonance imaging, diffusion-weighted magnetic resonance imaging, positron emission tomography, computed tomography, combined positron emission tomography computed tomography) or limited applicability (Doppler ultrasound).

In this study, we test the hypothesis that mid- to high-frequency ultrasound imaging and quantitative ultrasound (QUS) methods can be used to characterize tumor responses to cancer radiotherapy *in vivo*, as early as 24 hours after treatment administration. The ability to assess early tumor responsiveness to therapy within hours to days after the start of the treatment could ultimately aid clinicians in making decisions to modify therapy, e.g., choosing different radiation

Authors' Affiliations: Departments of [1]Medical Biophysics and [2]Radiation Oncology, University of Toronto, [3]Sunnybrook Health Sciences Centre, and [4]Department of Physics, Ryerson University, Toronto, Ontario, Canada; and [5]Orthopedics Department, Q-BAM Laboratory, University of Halle, Halle, Germany

Requests for reprints: Gregory J. Czarnota, Department of Radiation Oncology, Sunnybrook Health Sciences Centre, 2075 Bayview Avenue, Toronto, ON, Canada, M4N 3M5. Phone: 416-480-5329; Fax: 416-480-6002; E-mail: Gregory.Czarnota@sunnybrook.ca or Roxana M. Vlad, University Health Network, 101 College Street, Room 7-504, Toronto, Ontario, M5G 1L7 Canada. Phone: 416-581-7810; Fax: 416-480-6002; E-mail: Roxana.Vlad@sunnybrook.ca.

regimens, adding a radiosensitizer, or using different chemotherapy drugs that potentially could result in more effective treatment leading to improved outcomes and sparing patients from unnecessary side effects.

The aim of cancer therapy is to kill tumors by inducing cell death (10) that can be used as an indicator of tumor response to therapy (1, 11). Currently, standard methods for detecting cell death are invasive requiring tissue biopsy for histologic analysis. Previous studies have indicated that mid- to high-frequency ultrasound, i.e., 10 to 60 MHz, is sensitive to apoptosis *in vitro* and *in vivo*. Backscatter intensity from apoptotic cells has exhibited an up to 16-fold increase in comparison with viable cells (12, 13). In addition, spectral slopes (SS) have increased significantly for apoptotic cells compared with viable cells (13). Similar changes in ultrasound backscatter have been detected in tissues exposed to lethal ischemic injury (14). For the range of the ultrasound frequencies used in these studies, 10 to 60 MHz, the corresponding wavelengths of 150 to 25 μm, approach the size of cells and nuclei (10-20 μm) and, hence, are more sensitive to changes in cellular and nuclear structure than conventional ultrasound (frequencies, <10 MHz).

Characterization of tissue microstructure by examining frequency-dependent backscatter is termed QUS. QUS estimates describe the statistical properties of tissue structures or cell samples from a well-defined region of interest (ROI). QUS methods have been used to diagnose prostate cancer, ocular tumors, liver and cardiac abnormalities (15–18); differentiate benign fibroadenomas from mammary carcinomas and sarcomas (19); and have provided good diagnostic accuracy in prostate cancer detection and lesion localization (20). QUS methods, specifically spectral parameters, can be used to detect structural alterations induced by ultrasonically induced hyperthermia in tumor xenografts (21), discern between different types of ocular tumors (22, 23), and classify these depending on their lethality potential (16, 24).

This study represents the first evidence of the use of ultrasound imaging and spectrum analysis to detect radiotherapy effects *in vivo* in preclinical tumor mouse models. Tumor responses to radiotherapy were characterized by three ultrasound spectral parameters: the ultrasound-integrated backscatter (UIB), SS, and spectral intercept (SI). Although only two of these parameters are independent, it is useful to consider all three because each of them can be related to a different set of tissue scatterer properties. These spectral parameters were used, first, to compute the average ultrasound spectral parameters within a ROI and, second, to generate parametric images. We show that ultrasound spectral parameters and tumor parametric images can be used to noninvasively detect cell death in tumors, as early as 24 hours after radiotherapy at clinically relevant ultrasound frequencies of 10 to 30 MHz.

Materials and Methods

Animal use

All animal experiments were conducted in accordance with the guidelines of the Animal Care Committee (Sunnybrook Health Sciences Center) and satisfied all the rules for the humane use of laboratory animals. In all experiments, 6 to 8-wk-old severe combined
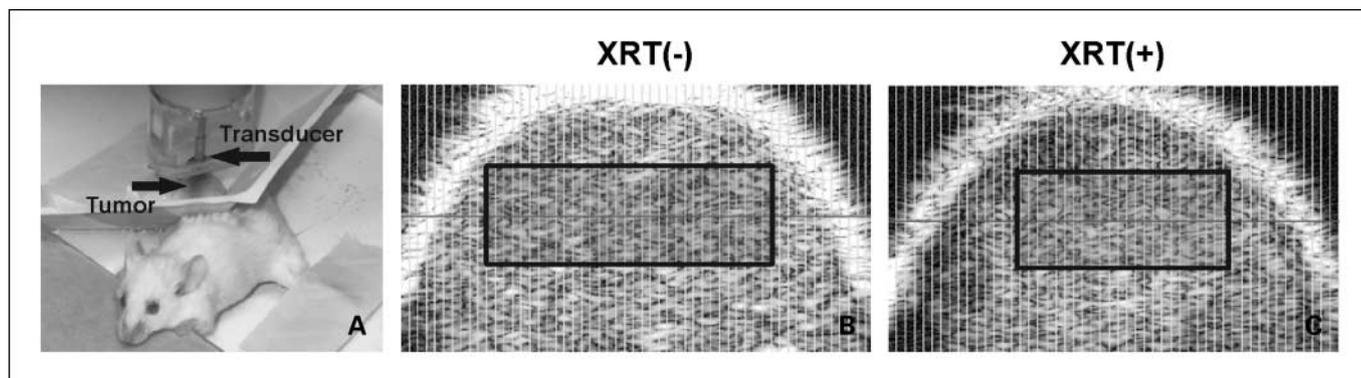
Fig. 1. The experimental setup for ultrasound data collection and representation of ROIs selection from ultrasound images. *A,* the mouse leg bearing the tumor was immersed in the coupling liquid (distilled and degassed water at room temperature) and data were collected from the entire tumor. *B* and *C,* ROIs were selected where the images seemed to be homogeneous with no interfaces or large echoes, 1 mm in height around the focal region of the transducer. *B,* for the XRT(-) tumors, the ROIs that met this condition were selected anywhere around the transducer focal zone; *C,* for the XRT(+) tumors, the ROIs were selected from the hyperechoic regions of the B-mode images. In this figure, the images seem to have similar backscattering intensity because of the gain applied to the RF data [e.g., 18 dB to XRT(-) and 10 dB to XRT(+) tumor].
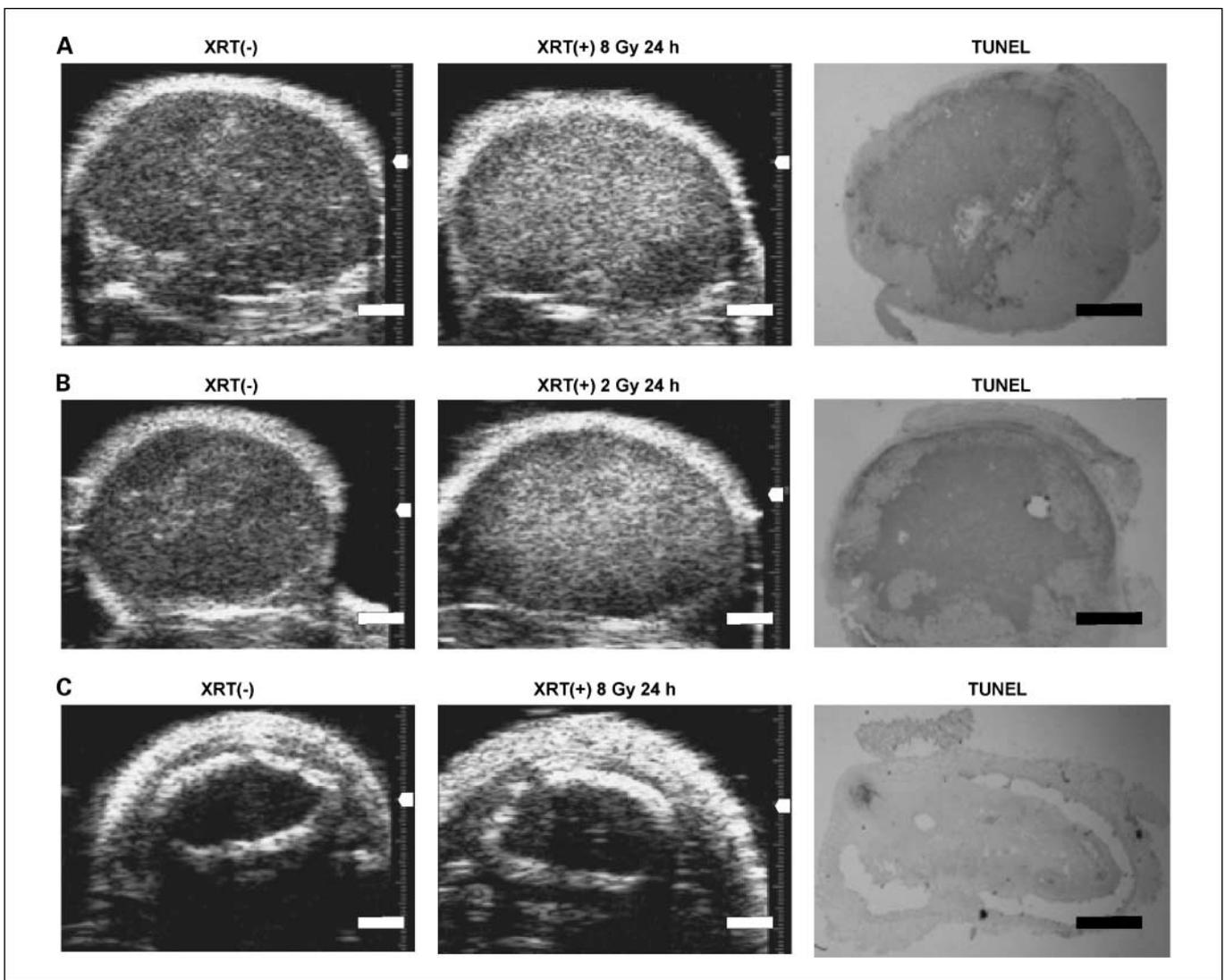
Fig. 2. Representative ultrasound images of the XRT(-) and XRT(+) tumors, and TUNEL staining corresponding to the XRT(+) tumors. *A* and *B,* ultrasound images of the C666-1 XRT(+) tumors presenting regions with increased echogeneity after radiotherapy, corresponding to the areas of cell death in the TUNEL-stained sections. *C,* Hep-2 tumor with no appreciable changes in the ultrasound images after exposure to radiotherapy and the corresponding TUNEL staining presenting only sparse brown spots indicating some isolated clusters of cell death. The white arrow on the lateral side of each tumor represents the location of the transducer focal point. *Scale bars,* 1 mm.

immunodeficient (SB-17) male mice (Charles River Laboratories, Inc.) were used.

Mouse tumors

Cell culture. Three mouse models of head and neck cancer, a nasopharyngeal carcinoma (C666-1), a squamous cell carcinoma of the pharynx (FaDu), and an epidermoid carcinoma of the larynx (Hep-2) were used in this study. FaDu and Hep-2 cell lines were obtained from American Type Culture Collection. C666-1 cells (25, 26) were maintained in RPMI 1640 cell culture media (Invitrogen Canada, Inc.) supplemented with 10% fetal bovine serum (Cansera International, Inc.) and antibiotics (100 mg/L penicillin and 100 mg/L streptomycin; Bioshop). FaDu cells were cultured in Eagle's minimum essential media (Invitrogen Canada, Inc.) with 2 mmol/L L-glutamine and Earle's balanced salt solution adjusted to contain 1.5 g/L sodium bicarbonate, 1.0 mmol/L sodium pyruvate (Sigma-Aldrich Co), and 10% fetal bovine serum. Hep-2 cells were cultured in minimum essential media supplemented with 10% fetal bovine serum and 0.1% gentamicin (Hoffman-La Roche Ltd). All cell lines were grown in a humidified atmosphere at 37°C, containing 5% CO_2.

Xenograft tumor models. C666-1 ($\sim 10^6$), Hep-2 ($\sim 10^6$), and FaDu ($\sim 10^5$) cells were injected intradermally into the left hind leg of each mouse. Primary tumors were allowed to develop for ~ 2 to 4 wk until they reached a diameter of 6 to 10 mm.

Before imaging, the mice were anesthetized and the tumors and surrounding area were depilated (Nair). Anesthesia consisted of 100 mg/kg ketamine, 5 mg/kg xylazine, and 1 mg/kg acepromazine typically in 0.1 mL saline injected i.v. This sedated the mice for ~ 1 h, sufficient time for the entire imaging and irradiation procedure. A total of 24 animals were used in this work. Six tumors per cell line were irradiated, with 2 animals at each radiation dose of 2, 4, and 8 Gy.[6] The notations used in this study are as follows: for the tumors prior the exposure to radiotherapy XRT(-) and for the tumors exposed to radiotherapy XRT(+). The rest of the animals served either as negative controls ($n = 4$), or the tumors exceeded the limit accepted for the experiment (10 mm largest dimension, $n = 2$). The histology of the

---

[6] The symbol Gy is Gray, the SI unit of absorbed radiation dose.
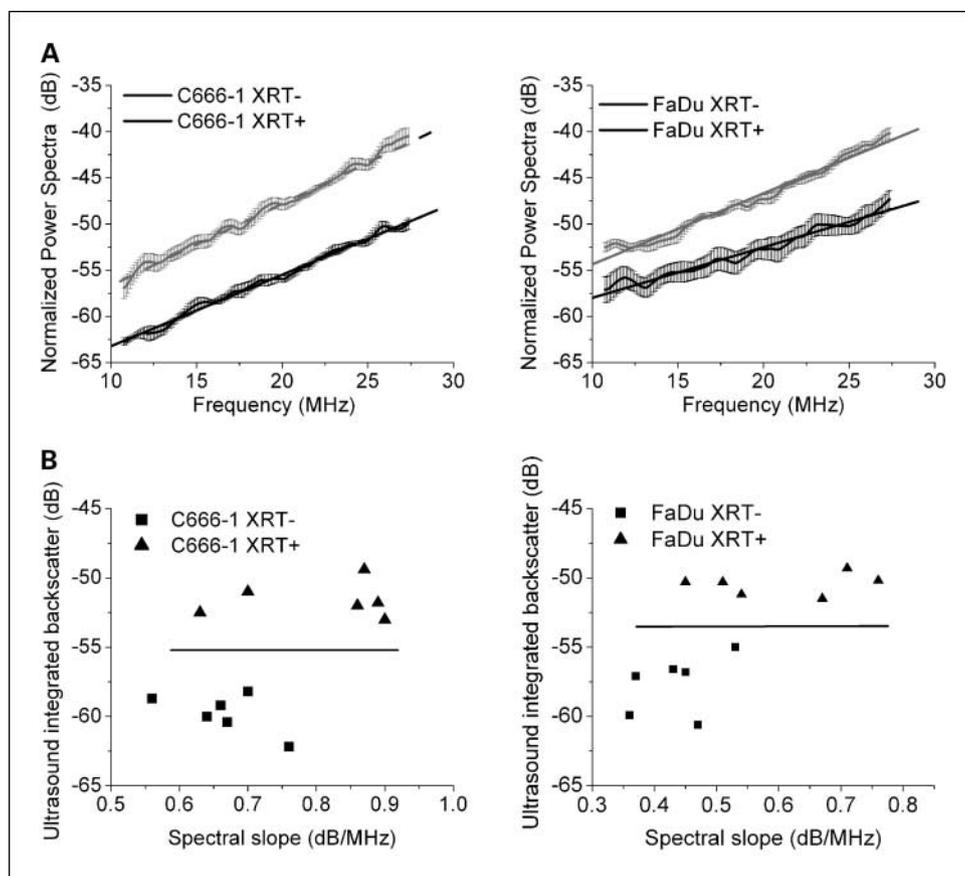
Fig. 3. Ultrasound spectral parameter characterization of tumor responses to radiotherapy. *A,* averaged NPS and SSs of C666-1 and FaDu tumors and, (*B*) corresponding feature analysis plots indicating a separation between the XRT(-) and XRT(+) tumors. *Error bars,* SE of the averaged spectra for animals (*n* = 6) per each tumor type (*A*).

negative control tumors was checked against the histology of those regions in XRT(+) tumors that did not respond to therapy. The large tumors exhibited large hyperechogenic patches in ultrasound images at day$_0$ and, therefore, were not considered as negative controls. These hyperechogenic patches were thought to represent regions of spontaneous cell death and, to check the histology of these patches, the large tumors followed the same protocol as the tumors exposed to radiotherapy (except irradiation).

Administration of ionizing radiation. Tumors were irradiated using a small animal irradiator (Faxitron Cabinet X-ray System; Faxitron X-ray Corporation) that delivered 160 keV X-rays at a rate of 200 cGy/minute.[7]

Ultrasound data acquisition and analysis

A VisualSonics VS40B high-frequency ultrasound device (Visual-Sonics, Inc.) with a 20-MHz focused transducer (20-mm focal length, 8-mm aperture diameter, -6 dB bandwidth of 11-28 MHz) was used to collect ultrasound images and radiofrequency (RF) data from all tumors. The experimental set-up is shown in Fig. 1A.

Data collection. Ultrasound images were collected from 10 to 20 different scan planes with a distance between planes of 0.5 mm, by scanning the whole tumor sequentially from one side to another to sample the entire tumor. RF data were collected from 5 to 10 different scan planes in the middle of the tumor. Each plane contained 40 to 60 8-bit RF lines sampled at 500 MHz. The ROIs chosen to calculate the average ultrasound parameters were 4- to 6-mm wide and 1 mm in height centered at the transducer focus, as displayed in Fig. 1B and C.

Spectrum analysis. RF data from each line segment were multiplied by a Hamming weighting function to suppress spectral lobes and the Fourier transform was computed. The squared magnitudes of the resultant spectra were averaged, divided by the power spectrum computed from a flat quartz to remove system and transducer transfer function and calculate the normalized power spectra (NPS). The resulting NPS were integrated over the -6 dB bandwidth of the transducer to calculate the averaged UIB (dB). The SS (dB/MHz), the slope calculated from the linear regression analysis of the NPS, and the SI (dB), the extrapolation at 0 MHz frequency, were computed. The UIB is similar to the midband fit described by the spectrum analysis framework developed by Lizzi et al. (27, 28) and can be related to the effective scatterer size, concentration, and difference in acoustic impedance between the scatterers and surrounding medium. The SS can be related to the effective scatterer[8] size (i.e., an increase in the SS corresponds in theory to a decrease in the effective scatterer size; ref. 29) and the SI depends on effective scatterer size, concentration, and relative acoustic impedance. Further details on the theoretical and signal analysis considerations and how spectral parameters are related to tissue microstructure can be found elsewhere (27, 28).

Because attenuation in intervening tissues can affect these parameters, the attenuation was separately estimated in skin and in tumor tissue, and the NPS were compensated for frequency-dependent attenuation in skin and tumor tissue. The attenuation coefficient assumed for the skin was 0.2 dB/mm/MHz based on published attenuation coefficients (30). The thickness of the skin was measured from the ultrasound images, yielding values of 0.30 ± 0.06 mm for XRT(-) and 0.45 ± 0.15 mm for XRT(+) tumors. The attenuation

---

[7] 1 cGy = 0.01 Gy.

[8] A tissue scatterer is a tissue constituent with different acoustic properties (acoustic impedance) than surrounding tissue.

coefficient used for the tumor tissue was 0.06 dB/mm/MHz. This value was computed in the homogeneous regions of the mouse tumors, before and 24 h after irradiation, by measuring the linear rate of decrease in UIB with increasing depth (17). This attenuation coefficient was similar to the attenuation coefficients measured *in vitro* from corresponding cell samples, viable and after exposure to radiotherapy (31). Signal analysis was done using custom programs developed in MATLAB (The Mathworks, Inc.).

Spectral parameter images. Parametric images were generated and displayed local values of UIB, SS, and SI as color-coded pixels. The images were formed using a sliding Hamming window of 500 μm with a 90% overlap to progressively analyze RF data along the individual scan lines. The length of the sliding window was chosen to yield parametric images with good resolution and reasonable stable estimates of spectral parameters based on the theoretical relationship between the size of the sliding window and the statistics of spectral parameters (32, 33). The spectrum analysis described above was done at each window site to compute the corresponding local parameter values.

Statistics. A *t* test was used to compare the spectral parameters computed from all independent RF lines collected from XRT(+) tumors against corresponding values computed from the same tumor before-irradiation XRT(-) using GraphPad Prism (GraphPad Software). A *P* value of <0.05 was considered significant.

Histology

Twenty-four hours after irradiation and immediately after final ultrasound imaging, tumors were excised, fixed in 10% neutral-buffered formalin, processed, and embedded in paraffin. Tumors were sectioned in the same nominal orientation to best match the ultrasound scanning planes. H&E staining was done for routine histologic analysis and terminal uridine deoxynucleotidyl transferase 2′-deoxyuridine 5′-triphosphate nick end labeling (TUNEL) staining was used to assess cell death, specifically apoptosis.

Results

Ultrasound images and spectral characterization results for all type of tumors are given in Figs. 2 to 4. Representative ultrasound images and corresponding TUNEL staining of C666-1 tumor sections before and 24 hours after irradiation are displayed in Fig. 2A and B. After exposure to different radiation doses, the tumors exhibited large hyperechoic patches corresponding to the brown-colored regions in the TUNEL staining indicating cell death. In contrast, Hep-2 tumors did not respond to therapy. Moreover, the tumors presented no significant change in echogenic appearance (Fig. 2C). TUNEL staining presented some isolated clusters of cell death after treatment with 8 Gy radiation dose (Fig. 2C) and no indication of cell death at 2 and 4 Gy radiation dose.

The average UIB measured from C666-1 and FaDu tumors increased by 8.2 ± 0.8 dB and 6.5 ± 1.0 dB ($P < 0.001$), respectively, after exposure to radiotherapy (Fig. 3A). The average SS increased from 0.77 ± 0.03 dB/MHz to 0.90 ± 0.05 dB/MHz for C666-1 tumors ($P < 0.05$) and from 0.54 ± 0.06 dB/MHz to 0.78 ± 0.05 dB/MHz for FaDu tumors ($P < 0.05$; Fig. 3A). A feature analysis plot of the UIB versus SS displayed a separation between the XRT(-) and XRT(+) tumors (Fig. 3B).

Some of the FaDu tumors exhibited small hyperechoic patches at day_0, as presented in Fig. 4A. We considered that this complex ultrasound pattern might correspond to
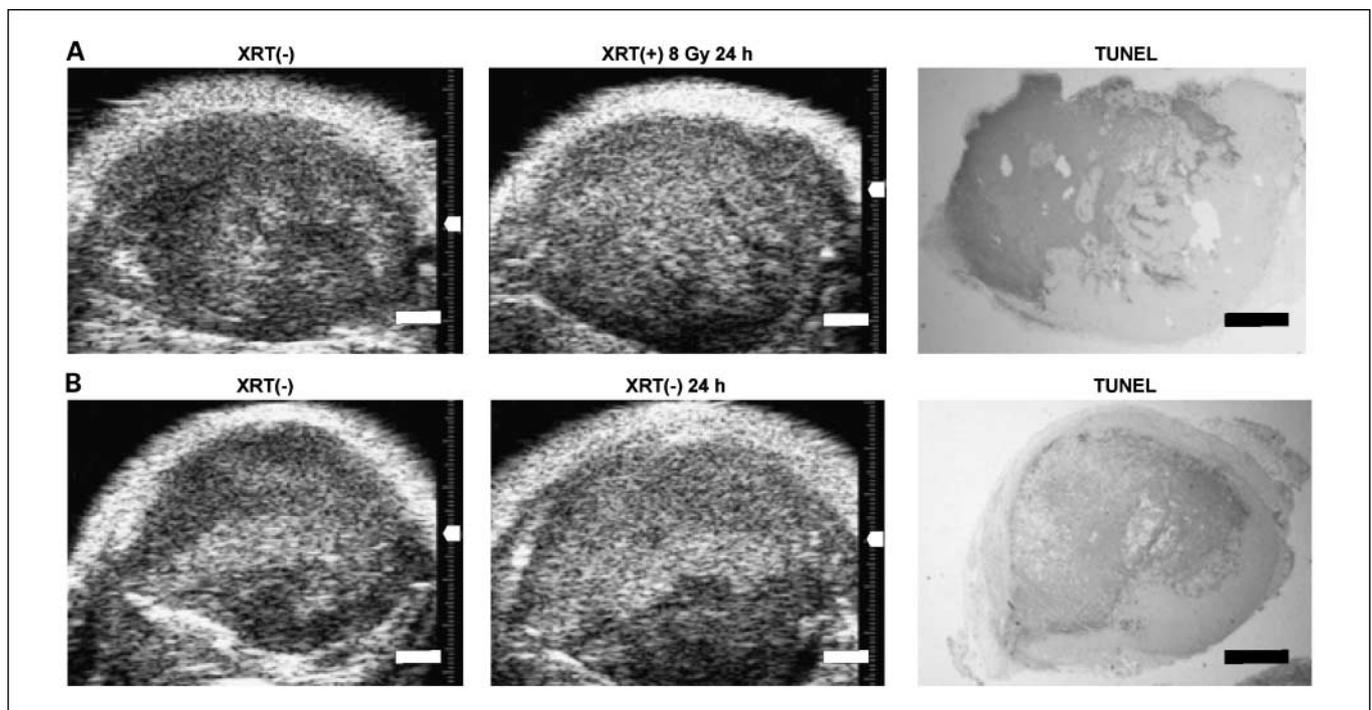
Fig. 4. Representative ultrasound images and corresponding TUNEL staining of FaDu tumors. *A,* FaDu XRT(-) tumor presenting some hyperechoic regions before treatment that enlarged and increased in brightness after exposure to radiotherapy, corresponding to the area of cell death in the TUNEL staining; (*B*) FaDu XRT(-) tumor presenting large hyperechoic regions at day_0, similar appearance after 24 h with no exposure to radiotherapy and corresponding TUNEL staining after 24 h indicating a large area of spontaneous cell death of similar shape as the hyperechoic area in the ultrasound image. The white spaces in this TUNEL staining represent histologic artifacts due to tissue retraction with fixation and specimen preparation procedures. These artifacts are typically more pronounced in the tissue regions presenting advanced cell death. The white arrow on the lateral side of each tumor represents the location of the transducer focal point. *Scale bars,* 1 mm.

small spontaneous necrotic/apoptotic regions inside the tumor before radiation exposure. This pattern would mimic well some human tumors, and hence, it was considered a valid approach to evaluate those tumors in the analysis. This pattern resulted in larger variability between NPS values calculated from XRT(-) FaDu tumors as indicated by Fig. 3A. Nevertheless, after radiotherapy, the size of the patches in these tumors increased, covering larger regions (Fig. 4A).

The tumors larger than 10 mm were not exposed to radiotherapy (Fig. 4B). These tumors exhibited large hyperechoic areas in the ultrasound images at day_0 and were kept in the experiment to histologically examine the nature of these hyperechogenic patches. These large, rapidly growing tumors increased in all three dimensions by 0.5 to 2 mm from day_0 to day_1, whereas the treated tumors did not present significant changes in size. No significant changes in the echogeneity of the ultrasound images of these untreated tumors were observed from day_0 to day_1. The corresponding TUNEL staining at day_1 exhibited a large area of cell death (Fig. 4B). This represents an example of ultrasound imaging detecting spontaneous cell death.

A representative ultrasound image, corresponding TUNEL staining, and parametric images computed from the local estimates of spectral parameters are displayed in Fig. 5. The local estimates of the UIB and SI were greater in the areas corresponding to the hyperechoic patches in the ultrasound images, following closely the areas of cell death from TUNEL staining (Fig. 5A-D). The parametric images constructed from the SS estimates resulted in a pattern of features different from the pattern in the corresponding conventional ultrasound images (Fig. 5A and E).

H&E staining revealed a clear delineation between the areas of cell death, characterized by small condensed and fragmented nuclei, and regions exibiting the normal phenotype (Fig. 6A and B). Overall the H&E staining revealed high tissue heterogeneity, more pronounced in the area of cell death and characterized by disparate nuclear sizes and changes in nuclear density. The area of viable cell phenotype contained some isolated clusters of cell death and exhibited a more homogeneous appearance (Fig. 6B and C). The H&E staining of the unirradiated tumor presented no significant evidence of cell death (Fig. 6C).

Discussion

This study shows for the first time that radiotherapy effects can be characterized by QUS methods in preclinical mouse cancer models, as early as 24 hours after treatment administration. The changes in ultrasound images and spectral parameters were interpreted as direct consequences of cell death after radiotherapy. This method was able to detect the regions of cell death in tumors and, thus, it has the potential to detect the tumors or tumor regions that respond to treatment from those that do not.

The histology from this study revealed that the most prominent structural changes after radiotherapy were related to cell nucleus as indicated by the TUNEL staining (Figs. 2, 4, and 5) and H&E staining (Fig. 6). These histologic observations and evidence from previous work (12, 13, 31, 34, 35) suggested that the main changes in the ultrasound backscatter after radiotherapy were related to changes in nuclear size and properties.

Changes in UIB can be related to a combination of scatterer properties: size, spatial organization, concentration, and relative acoustic impedance (28, 36). The regions exhibiting cell death in histology were characterized by an overall decrease in nuclear sizes, a consequence of nuclear condensation and fragmentation during the sequence of apoptotic cell death (Fig. 6). According to models of ultrasound scattering (23), a decrease in scatterer size alone, maintaining other factors constant, would result in a decrease in UIB. This was not observed in this work. Therefore, the changes in the UIB most likely resulted from a combination of changes in nuclear properties (i.e., changes in acoustic impedances, concentration, and spatial arrangement). For example, the darker staining of condensed nuclei suggested changes in the nuclear acoustic impedances, i.e., higher values of 2.00 MRayl for condensed chromatin versus 1.58 to 1.55 Mrayl for cytoplasm have been reported recently (37). The increase in the randomization of nuclei during the sequence of cell death may also contribute to the increase in the UIB as previously indicated by a model of ultrasound scattering (36) and, recently, suggested by experimental observations (31). Because SI is related to the size, concentration, and relative acoustic impedance of scatterers (27, 28), the increase in the SI, similar to the increase in the UIB, might result from changes in nuclear properties and increase in the number of nuclear fragments after apoptotic cell death.

The local estimates of the SS exhibited large variations in the regions that responded to therapy, as well as in the regions corresponding to the normal tumor phenotype (Fig. 5E). These variations may result from a combination of factors including the inherent biological heterogeneity of tissue structure, heterogeneity of the tumor response to treatment, and the model applied to calculate the SS estimates. The SS is mainly related to the scatterer size, therefore, the inherent biological variance of nuclear sizes and other structures affect the SS estimates. Furthermore, a recent study has indicated that there is an increase in the variance of nuclear and cellular sizes after cell death (31). This could further increase the local variability of the SS estimates, predominantly in the regions of the tumor that exhibit the characteristics of cell death. The SS estimates are frequency dependent, therefore, they are sensitive to the length of the sliding window and to the frequency-dependent attenuation. Larger sliding windows would yield better estimates and lower variance but with a compromise of a coarser resolution in the parametric images. Therefore, based on these considerations, the SS worked well in characterizing the responses to radiotherapy in large ROIs but yielded unstable local estimates when used with small ROIs. A variable attenuation along the ultrasound propagation path may also contribute to the larger variability of the local estimates of the SS. Further investigation toward the formulation of new models addressing the anisotropy of tissue constituents and their properties may help in obtaining better estimates for tissue characterization (37).

Implications. The head and neck cancer mouse models were chosen in this study because a primary treatment modality for these types of cancers is radiation therapy. Considering future applications of the technique described in this work, these types of tumors could be accessed in humans with endoscopic probes
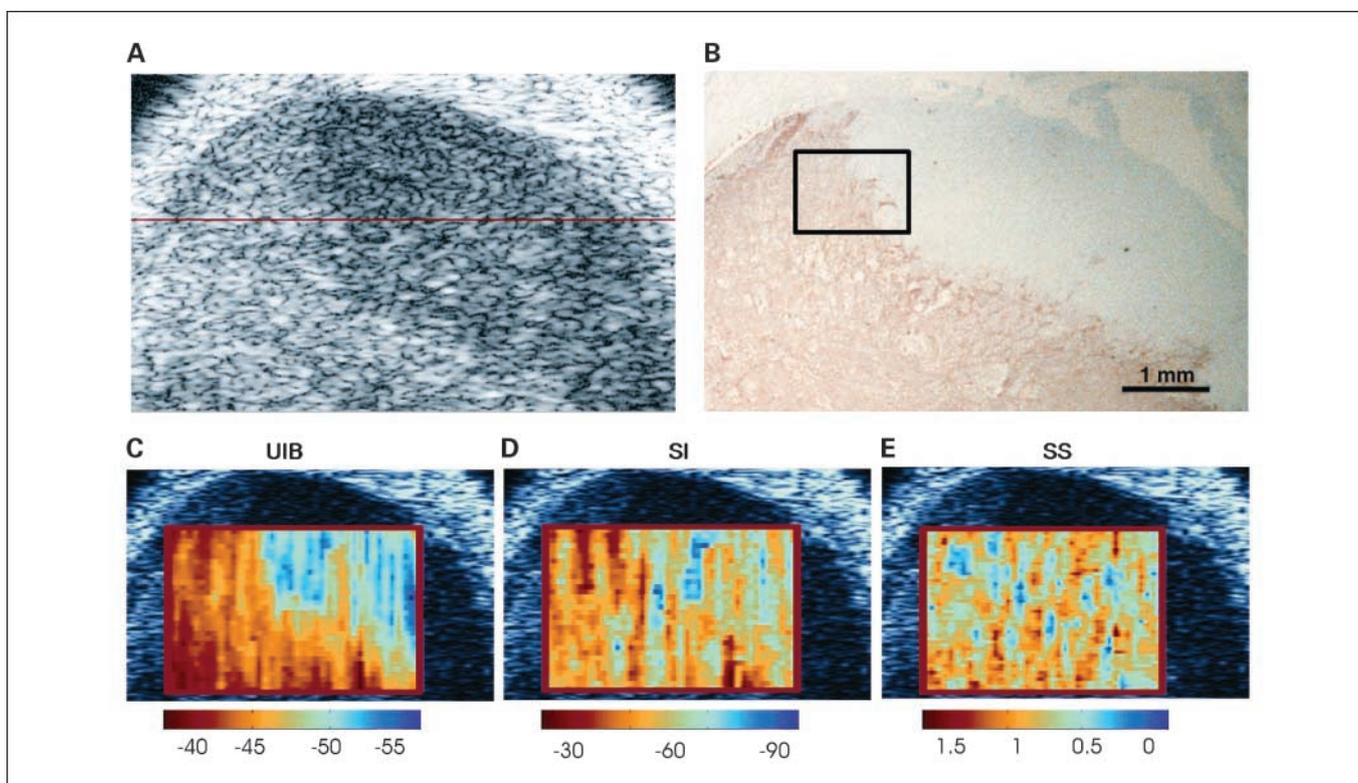
Fig. 5. Ultrasound image with corresponding histology and parametric images. *A,* ultrasound image, (*B*) corresponding TUNEL-stained image indicating an area of cell death of similar shape as the hyperechoic area in the ultrasound image and parametric images computed from the local estimates of (*C*) UIB, (*D*) SI, and (*E*) SS. The colorbars under each parametric image indicate the ranges of the corresponding estimates of the spectral parameters. The boxed region in the TUNEL staining corresponds to the H&E staining from the Fig. 6A.

working at 10 to 20 MHz (38). Ultrasound imaging enhanced by ultrasonic spectral parameters could provide a benefit of determining the tumor response early, within days after treatment starts. This would allow tumor imaging before and multiple times during treatment without the need of injecting specialized contrast agents as other techniques (e.g., positron emission tomography, dynamic contrast-enhanced magnetic resonance imaging, Doppler ultrasound). An early indicator of treatment response would be of great value to tailor treatments

to individual patients and particularly promising in multistage interventions or combination treatments.

Guiding tissue biopsies may be another area of interest. Although tissue biopsies provide important information regarding molecular pathology and thus tumor response, the sampled tissue may not adequately represent the heterogeneity of the tumors and, furthermore, cannot be sampled longitudinally. Superimposed parameter estimates on gray scale ultrasound images enable noninvasive assessment of cell death in
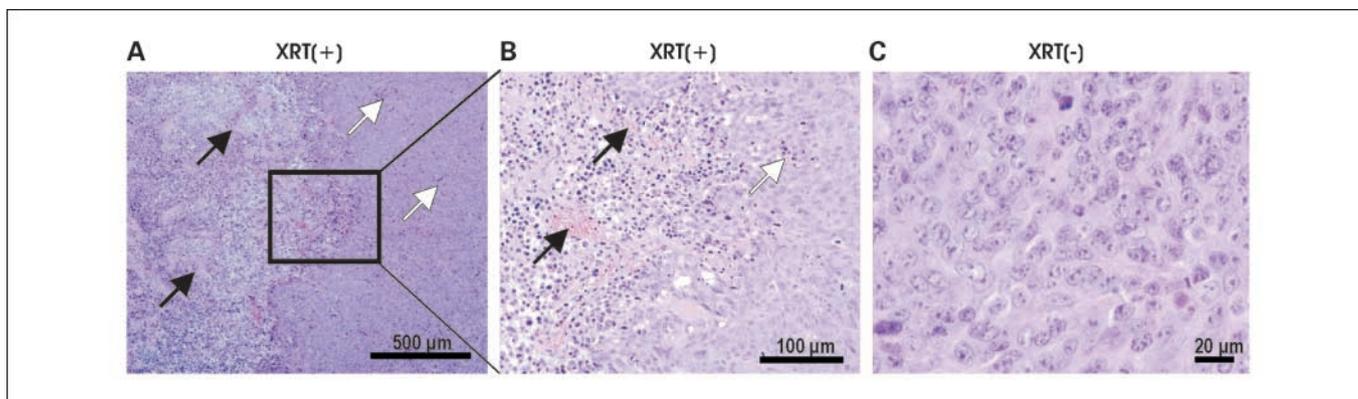
Fig. 6. H&E images of the XRT(+) tumor of Fig. 5 at two different magnifications (*A*) corresponding to the selection from Fig. 5B and *B* corresponding to the selection from *A* and H&E image (high magnification) of an XRT(-) tumor. The left side of the XRT(+) tumor images show the characteristics of cell death. The small white spaces in these regions represent histologic artifacts due to tissue retraction with fixation procedure. These artifacts are typically more pronounced in the tissue regions presenting advanced cell death. *Black arrows,* possible blood vessels. The right side of each image presents the appearance of viable tissue; *white arrows,* isolated clusters of cell death. *C,* The H&E image of the XRT(-) tumor exhibit a relative homogeneous appearance with no significant evidence of cell death.

tumor or tumor regions and can be used to determine the location for tissue biopsies.

Limitations. A penetration depth of 2 to 5 cm at the frequencies of 10 to 30 MHz allows the technique to be applicable to a variety of tumor types such as skin cancers, certain cancers of the breast, and cancers that can be reached with endoscopic probes such as nasopharyngeal and gastro-intestinal cancers. Ongoing studies in our laboratory are investigating the potential of detecting similar effects with lower frequency ultrasound of down to 5 MHz that may expand the range of applications (39).

In this work, the Hep-2 tumors did not respond to radiotherapy and presented no evidence of cell death in the TUNEL staining. Thus, the Hep-2 tumors served for two purposes in this study: to act as a tumor model that did not respond to radiotherapy and also to provide an example of a tumor model with a complex tissue structure not amenable to this type of ultrasound analysis due to high specular reflections at the interfaces with some tissue structures. These structures were highly attenuating and obscured the ultrasound scattering in the encapsulated tumor (Fig. 2C).

In conclusion, spectral parameters and tumor parametric images constructed from spectral parameters were used to detect responses to radiation treatment *in vivo* for two cancer mouse models, at 24 hours after treatment administration and at the clinically relevant frequencies of 10 to 30 MHz. The ultrasound imaging within this frequency range was also able to detect spontaneous cell death in large XRT(-) tumors. This validates our findings, indicating that this ultrasound detection method is sensitive to the structural changes after cell death.

The third tumor model did not respond to therapy as verified by TUNEL staining and provided an example of complex tumor pattern for which this type of analysis may not be applicable without additional assessment tools. The experimental evidence presented in this study supports the rationale for the application of mid- to high-frequency ultrasound imaging and QUS methods to characterize early tumor responses to cancer radiotherapy. The results indicate that these cell structural changes have a significant influence on spectral parameters providing a framework for future experiments and/or clinical studies aimed at demonstrating the potential of rapidly and noninvasively monitoring the effects of radiotherapy and other anticancer treatments using an ultrasound based approach.

Disclosure of Potential Conflicts of Interest

No potential conflicts of interest were disclosed.

Acknowledgments

References

1. Brindle K. New approaches for imaging tumour responses to treatment. Nat Rev Cancer 2008;8: 94–107.
2. Weber WA, Figlin R. Monitoring cancer treatment with PET/CT: Does it make a difference? J Nucl Med 2007;48:36–44S.
3. Erasmus JJ, Munden RF. The role of integrated computed tomography positron-emission tomography in esophageal cancer: staging and assessment of therapeutic response. Semin Radiat Oncol 2007; 17:29–37.
4. Brasch RC, Li KC, Husband JE, et al. *In vivo* monitoring of tumor angiogenesis with MR imaging. Acad Radiol 2000;7:812–23.
5. Preda A, Wielopolski PA, Ten Hagen TL, et al. Dynamic contrast-enhanced MRI using macromolecular contrast media for monitoring the response to isolated limb perfusion in experimental soft-tissue sarcomas. MAGMA 2004;17:296–302.
6. Tsien C, Gomez-Hassan D, Chenevert TL, et al. Predicting outcome of patients with high-grade gliomas after radiotherapy using quantitative analysis of T1-weighted magnetic resonance imaging. Int J Radiat Oncol Biol Phys 2007;67:1476–83.
7. DeVries AF, Kremser C, Hein PA, et al. Tumor micro-circulation and diffusion predict therapy outcome for primary rectal carcinoma. Int J Radiat Oncol Biol Phys 2003;56:958–65.
8. Theilmann RJ, Borders R, Trouard TP, et al. Changes in water mobility measured by diffusion MRI predict response of metastatic breast cancer to chemo-therapy. Neoplasia 2004;6:831–7.
9. Lassau N, Lamuraglia M, Vanel D, et al. Doppler US with perfusion software and contrast medium injection in the early evaluation of isolated limb perfusion of limb sarcomas: Prospective study of 49 cases. Ann Oncol 2005;16:1054–60.
10. Tannock IF, Hill RP, Bristow RG, Harrington L. The basic science of oncology. 4th ed. In: Tannock I, editor. New York: McGraw-Hill; 2005.
11. Symmans WF, Volm MD, Shapiro RL, et al. Paclitax-el-induced apoptosis and mitotic arrest assessed by serial fine-needle aspiration: Implications for early prediction of breast cancer response to neoadjuvant treatment. Clin Cancer Res 2000;6:4610–7.
12. Czarnota GJ, Kolios MC, Abraham J, et al. Ultra-sound imaging of apoptosis: High-resolution non-invasive monitoring of programmed cell death *in vitro, in situ* and *in vivo*. Br J Cancer 1999;81:520–1.
13. Kolios MC, Czarnota GJ, Lee M, Hunt JW, Sherar MD. Ultrasonic spectral parameter characterization of apoptosis. Ultrasound Med Biol 2002;28:589–97.
14. Vlad RM, Czarnota GJ, Giles A, Sherar MD, Hunt JW, Kolios MC. High-frequency ultrasound for monitoring changes in liver tissue during preservation. Phys Med Biol 2005;50:197–213.
15. Feleppa EJ, Kalisz A, Melgar S, et al. Typing of prostate tissue by ultrasonic spectrum analysis. IEEE Trans. Ultrason Ferroelec Freq Contr 1996;43:609–19.
16. Silverman RH, Folberg R, Rondeau MJ, et al. Spectral parameter imaging for detection of prognostically significant histologic features in uveal melanoma. Ultrasound Med Biol 2003;29:951–9.
17. Lizzi FL, King DL, Rorke MC, et al. Comparison of theoretical scattering results and ultrasonic data from clinical liver examinations. Ultrasound Med Biol 1988; 14:377–85.
18. Yang M, Krueger TM, Miller JG, Holland MR. Characterization of anisotropic myocardial backscatter using spectral slope, intercept and midband fit parameters. Ultrason Imaging 2007;29:122–34.
19. Oelze ML, O'Brien WD, Jr., Blue JP, Zachary JF. Differentiation and characterization of rat mammary fibroadenomas and 4T1 mouse carcinomas using quantitative ultrasound imaging. IEEE Trans Med Imaging 2004;23:764–71.
20. Feleppa EJ, Porter CR, Ketterling J, et al. Recent developments in tissue-type imaging (TTI) for planning and monitoring treatment of prostate cancer. Ultrason Imaging 2004;26:163–72.
21. Silverman RH, Coleman DJ, Lizzi FL, et al. Ultra-sonic tissue characterization and histopathology in tumor xenografts following ultrasonically induced hyperthermia. Ultrasound Med Biol 1986;12:639–45.
22. Coleman DJ, Lizzi FL, Silverman RH, Helson L, Torpey JH, Rondeau MJ. A model for acoustic characterization of intraocular tumors. Invest Ophthalmol Vis Sci 1985;26:545–50.
23. Shung KK, Thieme GA. Ultrasonic scattering in biological tissues, chapter 3. In: Shung KK, Thieme GA, editors. CRC Press; 1993.
24. Feleppa EJ, Lizzi FL, Coleman DJ, Yaremko MM. Diagnostic spectrum analysis in ophthalmology: A physical perspective. Ultrasound Med Biol 1986;12: 623–31.
25. Cheung ST, Huang DP, Hui AB, et al. Nasopharyngeal carcinoma cell line (C666–1) consistently harbouring epstein-barr virus. Int J Cancer 1999;83:121–6.
26. Li JH, Chia M, Shi W, et al. Tumor-targeted gene therapy for nasopharyngeal carcinoma. Cancer Res 2002;62:171–8.
27. Lizzi FL, Greenebaum M, Feleppa EJ, Elbaum M, Coleman DJ. Theoretical framework for spectrum analysis in ultrasonic tissue characterization. J Acoust Soc Am 1983;73:1366–73.
28. Lizzi FL, Astor M, Liu T, Deng C, Coleman DJ, Silverman RH. Ultrasonic spectrum analysis for tissue assays and therapy evaluation. Int J Imaging Syst Technol 1997;8:3–10.
29. Lizzi FL, Feleppa EJ, Kaisar AS, Deng CX. Ultrasonic spectrum analysis for tissue evaluation. Pattern Recognit Lett 2003;24:637–58.
30. Shung KK. Diagnostic ultrasound: Imaging and blood flow measurements. CRC Press; 2005. p. 155.

31. Vlad RM, Alajez NM, Giles A, Kolios MC, Czarnota GJ. Quantitative ultrasound characterization of cancer radiotherapy effects *in vitro*. Int J Radiat Oncol Biol Phys 2008;72:1236–43.

32. Lizzi FL, Astor M, Feleppa EJ, Shao M, Kalisz A. Statistical framework for ultrasonic spectral parameter imaging. Ultrasound Med Biol 1997;23:1371–82.

33. Lizzi FL, Alam SK, Mikaelian S, Lee P, Feleppa EJ. On the statistics of ultrasonic spectral parameters. Ultrasound Med Biol 2006;32:1671–85.

34. Taggart LR, Baddour RE, Giles A, Czarnota GJ, Kolios MC. Ultrasonic characterization of whole cells and isolated nuclei. Ultrasound Med Biol 2007;33:389–401.

35. Banihashemi B, Vlad RM, Giles A, Kolios MC, Czarnota GJ. Ultrasound imaging of apoptosis in tumour response: Novel monitoring of photodynamic therapy effects. Cancer Res 2008;68:8590–6.

36. Hunt JW, Worthington AE, Kerr AT. The subtleties of ultrasound images of an ensemble of cells: simulation from regular and more random distributions of scatterers. Ultrasound Med Biol 1995;21:329–41.

37. Mamou J, Oelze ML, O'Brien WD, Jr., Zachary JF. Identifying ultrasonic scattering sites from three-dimensional impedance maps. J Acoust Soc Am 2005;117:413–23.

38. Lightdale CJ, Kulkarni KG. Role of endoscopic ultrasonography in the staging and follow-up of esophageal cancer. J Clin Oncol 2005;23:4483–9.

39. Czarnota GJ, Papanicolau N, Lee J, Karshafian R, Giles A, Kolios MC. Novel low-frequency ultrasound detection of apoptosis *in vitro* and *in vivo* [abstract]. Ultrason Imaging 2008;29:237–8.